# Multidimensional MRI for characterization of subtle axonal injury accelerated using an adaptive nonlocal multispectral filter

**Dan Benjamini** [1,2,3,*], **Mustapha Bouhrara** [4], **Michal E. Komlosh** [1,2,3], **Diego Iacono** [3,5−9], **Daniel P. Perl** [5,7], **David L. Brody** [2,10], **and Peter J. Basser** [1,2]

[1] *Section on Quantitative Imaging and Tissue Sciences, National Institute of Child Health and Human Development, National Institutes of Health, Bethesda, MD, USA*
[2] *Center for Neuroscience and Regenerative Medicine, Uniformed Services University of the Health Sciences, Bethesda, MD, USA*
[3] *The Henry M. Jackson Foundation for the Advancement of Military Medicine (HJF), Bethesda, MD, USA*
[4] *Magnetic Resonance Physics of Aging and Dementia Unit, National Institute of Aging, National Institutes of Health, Baltimore, MD, USA*
[5] *Brain Tissue Repository & Neuropathology Program, Uniformed Services University (USU), Bethesda, MD, USA*
[6] *Department of Neurology, F. Edward Hébert School of Medicine, Uniformed Services University, Bethesda, MD, USA*
[7] *Department of Pathology, F. Edward Hébert School of Medicine, Uniformed Services University, Bethesda, MD, USA*
[8] *Department of Anatomy, Physiology and Genetics, F. Edward Hébert School of Medicine, Uniformed Services University, Bethesda, MD, USA*
[9] *Neurodegeneration Disorders Clinic, National Institute of Neurological Disorders and Stroke, National Institutes of Health, Bethesda, MD, USA*
[10] *Laboratory of Functional and Molecular Imaging, National Institute of Neurological Disorders and Stroke, National Institutes of Health, Bethesda, MD, USA*

Correspondence*:
Dan Benjamini, National Institute of Child Health and Human Development, National Institutes of Health, Bethesda, MD, 20814, USA
dan.benjamini@nih.gov

## ABSTRACT

Multidimensional MRI is an emerging approach that simultaneously encodes water relaxation ($T_1$ and $T_2$) and mobility (diffusion) and replaces voxel-averaged values with subvoxel distributions of those MR properties. While conventional (i.e., voxel-averaged) MRI methods cannot adequately quantify the microscopic heterogeneity of biological tissue, using subvoxel information allows to selectively map a specific $T_1$-$T_2$-diffusion spectral range that corresponds to a group of tissue elements. The major obstacle to the adoption of rich, multidimensional MRI protocols for diagnostic or monitoring purposes is the prolonged scan time. Our main goal in the present study is to evaluate the performance of a nonlocal estimation of multispectral magnitudes (NESMA) filter on reduced datasets to limit the total acquisition time required for reliable multidimensional MRI characterization of the brain. Here we focused and reprocessed results from a recent study that identified potential imaging biomarkers of axonal injury pathology from the joint analysis of multidimensional MRI, in particular voxelwise $T_1$-$T_2$ and diffusion-$T_2$ spectra in human Corpus

Callosum, and histopathological data. We tested the performance of NESMA and its effect on the accuracy of the injury biomarker maps, relative to the co-registered histological reference. Noise reduction improved the accuracy of the resulting injury biomarker maps, while permitting data reduction of 35.7% and 59.6% from the full dataset for $T_1$-$T_2$ and MD-$T_2$ cases, respectively. As successful clinical proof-of-concept applications of multidimensional MRI are continuously being introduced, reliable and robust noise removal and consequent acquisition acceleration would advance the field towards clinically-feasible diagnostic multidimensional MRI protocols.

**Keywords: multidimensional, MRI, diffusion, relaxation, traumatic brain injury, axonal injury, multispectral nonlocal filtering, NESMA**

## 1 INTRODUCTION

Water molecules within biological tissues interact with their local chemical environment via nuclear relaxation processes and follow diffusion patterns trajectories that are governed by the local tissue density and geometry. Using a combination of magnetic field profiles to probe these mechanisms, magnetic resonance (MR) provides exquisite sensitivity to both the chemical composition, through relaxation parameters, and microstructure, through diffusion parameters, of biological tissues.

One fundamental obstacle for using MRI to characterize tissue heterogeneity is the averaging that occurs across the image volume elements, known as voxels (i.e., pixels with thickness). Voxel-averaged images can only provide macroscopic information with respect to the voxel size, which is typically $\sim$1-3 mm$^3$. In a mammalian brain, an individual voxel contains multiple chemical and physical microenvironments such as axons, neurons, glia, myelin, and cerebrospinal fluid. Many biological processes-of-interest take place at a microscopic scale that only affects a small portion of any given voxel, which therefore makes them undetectable using conventional voxel-averaged MRI methods. The inability to separate normal and pathological tissue within a voxel is a major contributor to the insensitivity and ensuing non-specificity of conventional MRI methods in detecting abnormal cellular processes.

By simultaneously encoding multiple MR "dimensions", such as relaxation times ($T_1$ and $T_2$) [1] and diffusion [2, 3], multidimensional distributions of those MR parameters can provide fingerprints of various chemical and physical microenvironments within the volume-of-interest, which can be traced back to specific materials and cellular components. If combined with imaging [4], multidimensional MRI has the potential to overcome the voxel-averaging limitation by accomplishes two fundamental goals: (1) it provides unique intra-voxel distributions instead of an average over the whole voxel; this allows identification of multiple components within a given voxel [5, 6, 7], while (2) the multiplicity of dimensions inherently facilitates their disentanglement; this allows higher accuracy and precision in derived quantitative values [8, 9, 10, 11].

Although traditionally multidimensional MR experiments required many repeated acquisitions and therefore have imposed serious time constraints [12], acquisition strategy [13, 14], computational [15, 6, 3], and pulse design [16] technological breakthroughs have significantly reduced the data burden and positioned multidimensional MRI as a powerful emerging imaging modality for studying biological media. Despite of these advances, wide-spread clinical translation still presents challenges, in particular, due to relatively low signal-to-noise ratio (SNR) and the ensuing increased data amount requirement. To address that, we report the use of a nonlocal estimation of multispectral magnitudes (NESMA) filter [17] on multidimensional MRI data to perform noise reduction for reliable parameter determination and further data reduction. To date, NESMA has been successfully used to improve determination of myelin water fraction from multi-spin-echo MR images [18], or cerebral blood flow from arterial spin labeling MR images [19].

We chose to focus and reprocess a subset of data from our recent study that showed multidimensional MRI can uncover subtle axonal injury patterns in the human brain, otherwise inaccessible using conventional quantitative MRI techniques such as diffusion tensor imaging (DTI), $T_1$ or $T_2$ maps [20]. The study investigated brain samples derived from human subjects who had sustained traumatic brain injury (TBI) and control brain donors using MRI, followed by co-registered histopathology that included amyloid precursor protein (APP) immunoreactivity to define axonal injury severity [21]. Abnormal multidimensional $T_1$-$T_2$, mean diffusivity-$T_2$ (MD-$T_2$), and MD-$T_1$ spectral signatures that were strongly associated with injured voxels were identified and used to generate axonal injury biomarker maps [20]. Here we study the effect of applying a multispectral nonlocal filter on three representative cases (a control and two TBI cases), with the main goal of evaluating the performance of NESMA on reduced datasets to limit the total acquisition time required for reliable multidimensional MRI characterization of brain tissue.

## 2 METHOD

### 2.1 Donors specimens employed in the present study

We evaluated autopsy-derived brain specimens from two different human brain collections. Formalin-fixed portions of approximately 20x20x10 mm$^3$ of the Corpus Callosum (CC) were obtained from one military subject from the DoD/USU Brain Tissue Repository and Neuropathology Program (https://www.researchbraininjury.org, Bethesda, MD; Subject 1), and two civilian subjects enrolled in the Transforming Research and Clinical Knowledge in Traumatic Brain Injury study (TRACK-TBI; https://tracktbi.ucsf.edu/transforming-research-and-clinical-knowledge-tbi) (Subjects 2 and 3). For each case, a next–of-kin or legal representative provided a written consent for donation of the brain for use in research. The brain tissues used have undergone procedures for donation of the tissue, its storage, and use of available clinical information that have been approved by the USU Institutional Review Board (IRB) prior to the initiation of the study. All experiments were performed in accordance with current federal, state, DoD, and NIH guidelines and regulations for postmortem analysis.

Subject 1 was a 44 years old male with no known TBI history and postmortem APP-negative histopathology. Subject 2 was a 60 year old male that died as a result of a intraparenchymal hemorrhage following a motor vehicle accident. Subject 3 was a 49 year old male that died as a result of intraparenchymal and subarachnoid hemorrhages following a fall.

### 2.2 MRI acquisition

Prior to MRI scanning, each formalin-fixed brain specimen was transferred to a phosphate-buffered saline (PBS) filled container for 12 days to ensure that any residual fixative was removed from the tissue. The specimen was then placed in a 25 mm tube, and immersed in perfluoropolyether (Fomblin LC/8, Solvay Solexis, Italy), a proton free fluid void of a proton-MRI signal. Specimens were imaged using a 7 T Bruker vertical bore MRI scanner equipped with a microimaging probe and a 25 mm quadrupole RF coil.

Multidimensional data were acquired using a 3D echo planar imaging (EPI) sequence with a total of 56 and 302 images for $T_1$-$T_2$ and MD-$T_2$, respectively, and with 300 $\mu$m isotropic spatial resolution, which resulted in respective acquisition times of 4.5 and 17.8 hr. Further details can be found in [20] and in the Supplementary Material.

To test the feasibility of data reduction using NESMA we derived reduced datasets by sub-sampling the full datasets in the following manner: (1) reducing the 1D encoding data by a factor of two, and in the MD-$T_2$ dataset (2) reducing the number of echo times by a factor of two, and the number of b-values from four to three. The total number of $T_1$-$T_2$ images was therefore reduced from 56 to 36 (35.7% decrease), while the total number of MD-$T_2$ images was reduced from 302 to 122 (59.6% decrease).

The SNR was always maintained above 100 (defined as the ratio between the average unattenuated signal intensity within a tissue region of interest, and the standard deviation of the signal intensity within the background). The sample temperature was set at 16.8°C.

### 2.3 Multidimensional MRI processing

Here we implemented a marginally-constrained, $\ell_2$-regularized, nonnegative least square optimization to compute the multidimensional distribution in each voxel, as previously described [8, 22]. It is a well-tested approach that had been proved robust and reliable [23, 24, 25, 2, 26, 27, 14], which in this study had resulted in two types of distributions in each voxel: $T_1$-$T_2$ and MD-$T_2$. The 2D $T_1$-$T_2$ and MD-$T_2$ distributions were evaluated on $50 \times 50$ logarithmically sampled grids using a previously described algorithm [13]. The range for $T_1$ was 1 – 10,000 ms, the range for $T_2$ was 1 – 500 ms, and the range for MD was 0.0001 – 5 $\mu$ m$^2$/ms.

If one considers the multidimensional distributions as spectra, it is possible to use them to generate maps of specific spectral components by means of integration over a predefined parameter range generally associated with a spectral peak. The integral value is a number between 0 and 1, representing a certain spectral component (SC) in a given multidimensional distribution, which can be computed in each voxel to generate an image of that specific SC [28]. Here we apply a recently proposed unsupervised algorithm to identify the injury-associated spectral information [20], and generate injury biomarker maps that closely follow APP histopathology.

### 2.4 The nonlocal estimation of multispectral magnitudes (NESMA) filter

For each sample, the multidimensional distributions were derived from the original multidimensional data as well as from data denoised using the NESMA filter to improve accuracy and precision in derived distributions. Briefly, NESMA restores the amplitude of an index voxel by incorporating the intensities of voxels with similar multispectral signal patterns, that is, intensities from multidimensional images. The similarity between two voxels across these images is calculated using the relative Euclidean distance within a large search window centered on the index voxel. The size of the search window must be sufficiently large to ensure inclusion of an adequate number of similar voxels, and sufficiently restricted to ensure that the transmission and reception radiofrequency fields and noise standard deviation are approximately constant within the window. Based on previous studies [29] and the isotropic voxel size, NESMA was implemented here using a search window size of $11 \times 11 \times 11$. Voxels exhibiting relative Euclidean distance lower than 5% are considered as being similar to the index voxel [17, 29].

### 2.5 Histopathology

After MRI scanning, each CC tissue block was transferred for histopathological processing. Tissue blocks from each brain specimen was processed using an automated tissue processor (ASP 6025, Leica Biosystems, Nussloch, Germany). After tissue processing, each tissue block was embedded in paraffin and cut in a series of 5 $\mu$m-thick consecutive sections on which immunohistochemistry for anti-amyloid precursor protein (APP) was performed (DS9800, Leica Biosystems, Buffalo Grove, IL). Further details can be found in [20].

## 3 RESULTS

We first investigated the spatially-resolved subvoxel $T_1$-$T_2$ and MD-$T_2$ spectral components to assess the effect of NESMA on the derived voxelwise spectra. To do that, it is useful to summarize the 4D information, which consists of 2D images with $50 \times 50$ spectra in each voxel, as arrays of images with varying subvoxel $T_1$, $T_2$, and MD values. To make them more readable, the $50 \times 50$ spectra were sub-sampled on a $10 \times 10$ grid. These maps are shown in Figs. 1, 2, and 3 for all three Subjects. Corresponding histological

APP images (co-registered with the MRI) are shown on the left panel of Fig. 4, with red color indicating abnormal APP accumulation.

Starting with the control case (Subject 1), the spatially-resolved subvoxel $T_1$-$T_2$ and MD-$T_2$ spectral components are shown in Fig. 1. The left column shows the results from the unfiltered data ($T_1$-$T_2$ and

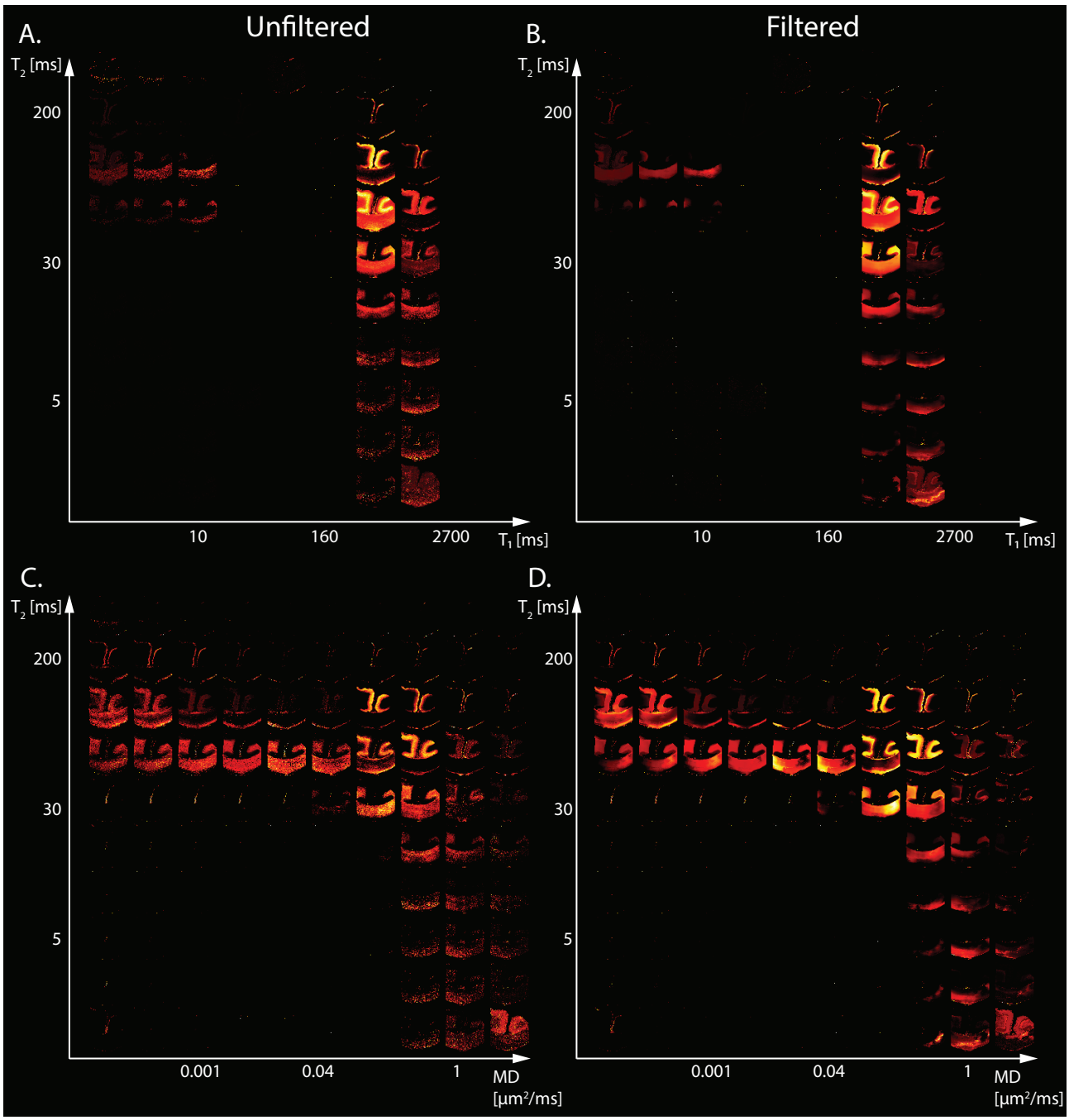


**Figure 1.** Maps of 2D probability density functions (i.e., 2D normalized spectra) from Subject 1 (control) of (A) unfiltered and (B) filtered subvoxel $T_1$-$T_2$ values reconstructed on a $10 \times 10$ grid of subvoxel $T_1$ values (horizontal axes) and subvoxel $T_2$ values (vertical axes), and maps of (C) unfiltered and (D) filtered subvoxel MD-$T_2$ values reconstructed on a $10 \times 10$ grid of subvoxel MD values (horizontal axes) and subvoxel $T_2$ values (vertical axes).

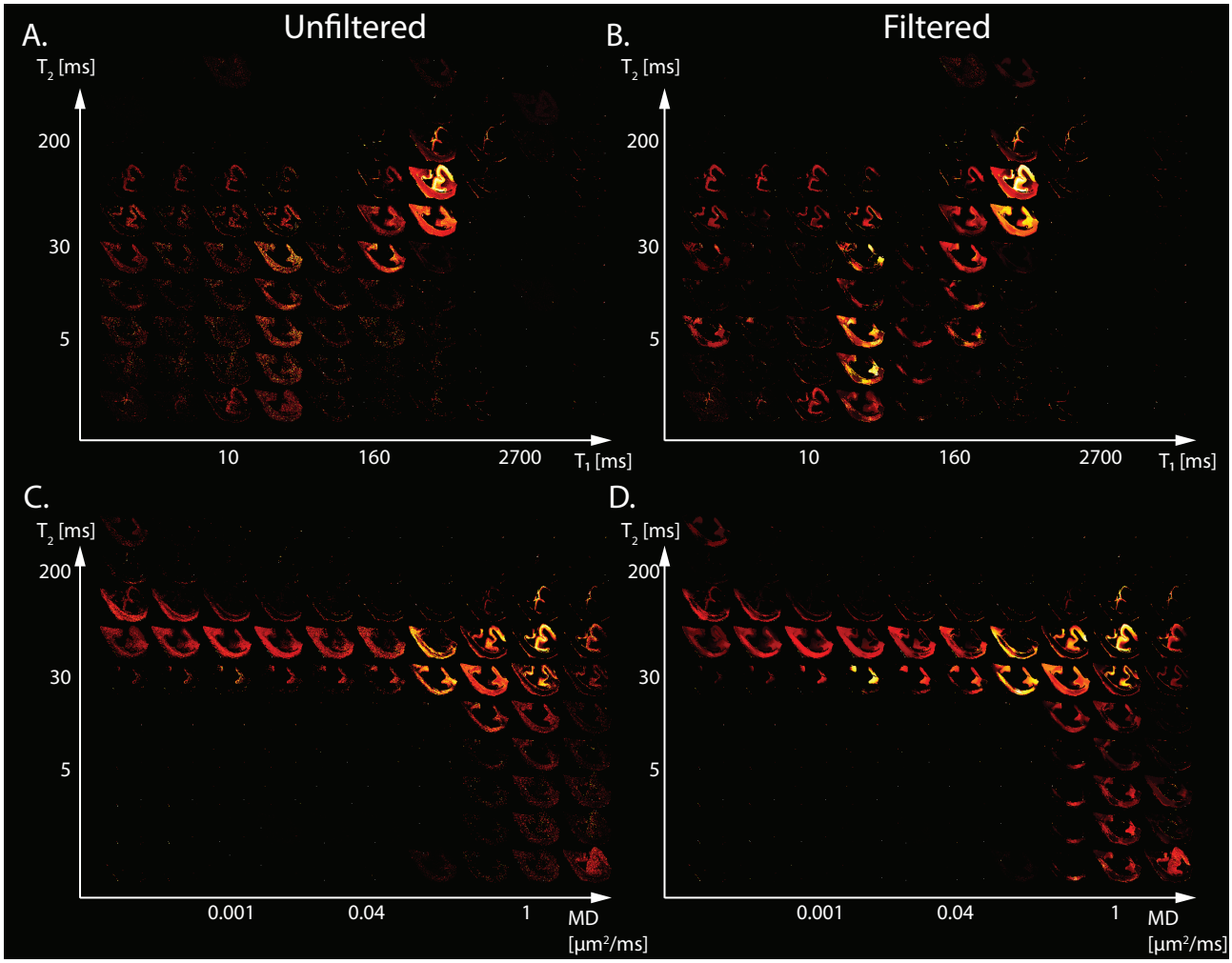


**Figure 2.** Maps of 2D probability density functions (i.e., 2D normalized spectra) from Subject 2 (TBI) of (A) unfiltered and (B) filtered subvoxel $T_1$-$T_2$ values reconstructed on a $10 \times 10$ grid of subvoxel $T_1$ values (horizontal axes) and subvoxel $T_2$ values (vertical axes), and maps of (C) unfiltered and (D) filtered subvoxel MD-$T_2$ values reconstructed on a $10 \times 10$ grid of subvoxel MD values (horizontal axes) and subvoxel $T_2$ values (vertical axes).

MD-$T_2$ in Figs. 1A and C, respectively), while the right column shows the results from the filtered data ($T_1$-$T_2$ and MD-$T_2$ in Figs. 1B and D, respectively). The maps revealed signal components that were spatially consistent with specific tissue types such as white matter and gray matter.

The spatially-resolved subvoxel $T_1$-$T_2$ and MD-$T_2$ spectral components from the first TBI case (Subject 2) are shown in Fig. 2. As before, the left column shows the results from the unfiltered data ($T_1$-$T_2$ and MD-$T_2$ in Figs. 2A and C, respectively), and the right column shows the results from the filtered data ($T_1$-$T_2$ and MD-$T_2$ in Figs. 2B and D, respectively). Similarly to the control case, here too the maps revealed signal components that were spatially consistent with specific tissue types.

The spatially-resolved subvoxel $T_1$-$T_2$ and MD-$T_2$ spectral components from the second TBI case (Subject 3) are shown in Fig. 3. Unfiltered ($T_1$-$T_2$ and MD-$T_2$ in Figs. 3A and C, respectively) and filtered data ($T_1$-$T_2$ and MD-$T_2$ in Figs. 3B and D, respectively) are shown. As before, signal components that were spatially consistent with specific tissue types as a function of $T_1$, $T_2$, and MD were revealed.

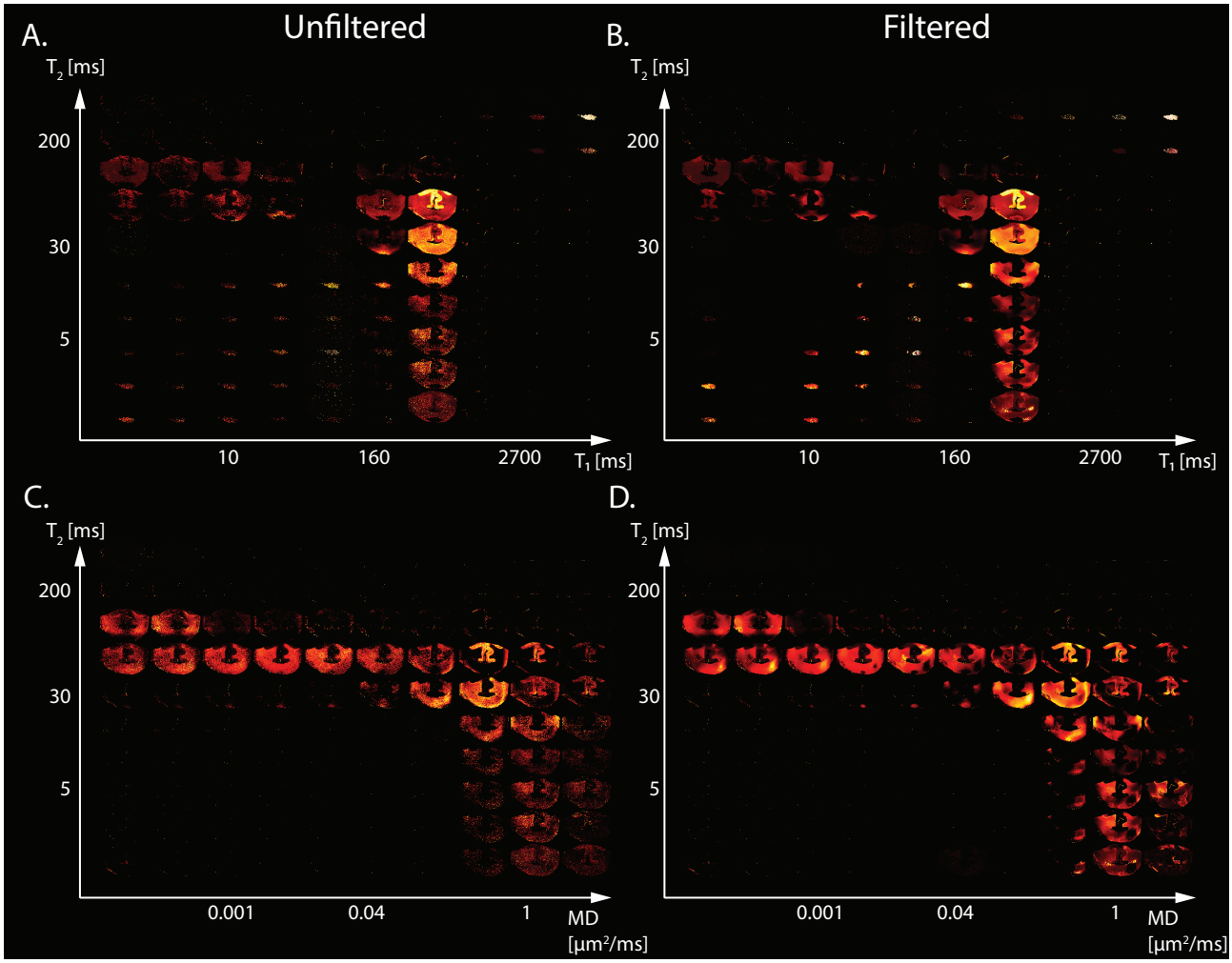


**Figure 3.** Maps of 2D probability density functions (i.e., 2D normalized spectra) from Subject 3 (TBI) of (A) unfiltered and (B) filtered subvoxel $T_1$-$T_2$ values reconstructed on a $10 \times 10$ grid of subvoxel $T_1$ values (horizontal axes) and subvoxel $T_2$ values (vertical axes), and maps of (C) unfiltered and (D) filtered subvoxel MD-$T_2$ values reconstructed on a $10 \times 10$ grid of subvoxel MD values (horizontal axes) and subvoxel $T_2$ values (vertical axes).

Figure 4 shows histological images and multidimensional MR-derived injury biomarker maps of the three representative cases. Histological images (red = APP stain) of the control case (Subject 1) show negative APP staining, compared with positive APP staining in the injured samples (Subjects 2 and 3). We then examine separately the two MRI-derived injury biomarkers, $T_1$-$T_2$ and MD-$T_2$, and show the resulting images obtained using the unfiltered full dataset (as originally published in [20]), the filtered full dataset, and the filtered reduced dataset. In addition, the MRI-derived injury biomarkers obtained by using the unfiltered reduced dataset are shown in Fig. S1 in the Supplementary Material.

Visual inspection of the different injury biomarker maps shown in Figs. 4 and S1 revealed that filtering of the data does not result in loss of the spectral information of interest, and furthermore, the filtered images appear qualitatively of higher quality. Importantly, the data reduction in the case of the filtered data did not significantly affect the resulting injury biomarker maps (Fig. 4). Evaluation of filtering performance was based upon the extent of noise reduction and feature preservation, and was quantified by computing the structural similarity index (SSIM) values [30] between the injury biomarker maps under the different

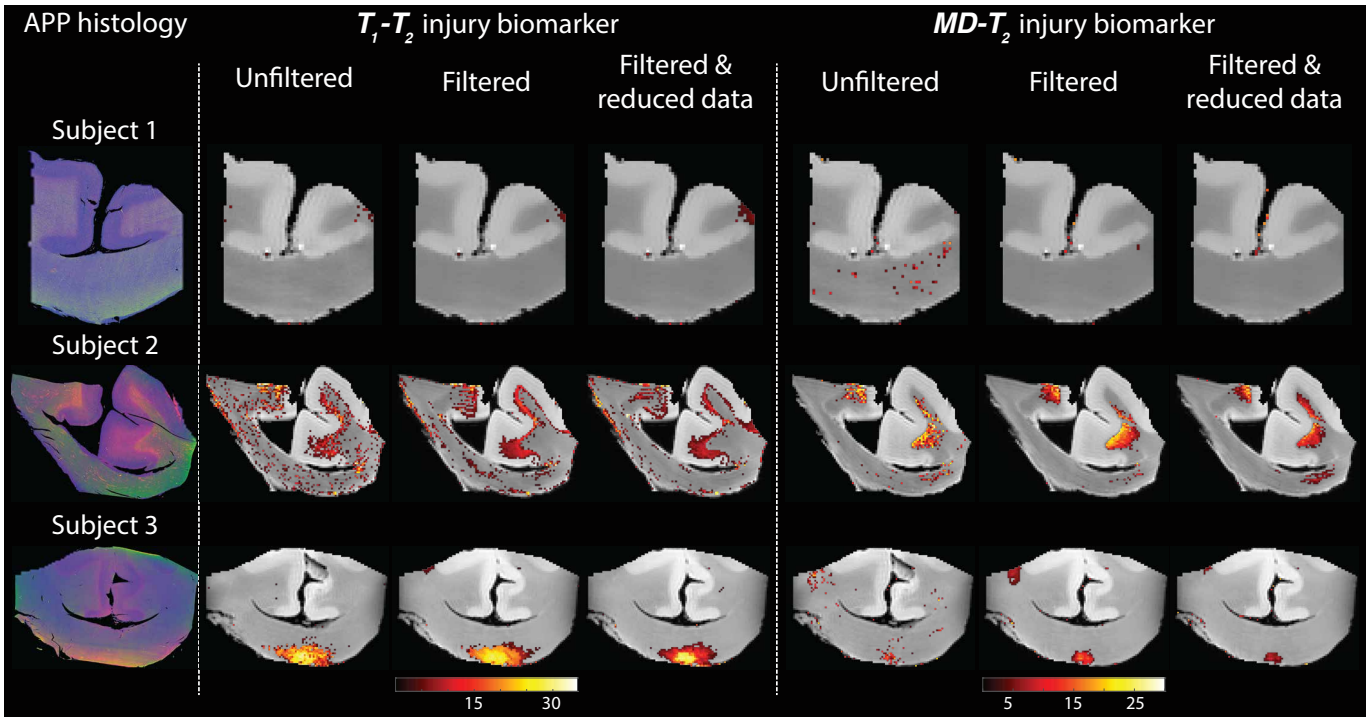


**Figure 4.** Histological images and multidimensional MR-derived injury biomarker maps of three representative cases, and under different conditions (left to right: unfiltered, filtered, and filtered & reduced data). Deconvolved histological APP images (co-registered with the MRI) are shown on the left panel, red = APP stain (top to bottom: control, and two TBI cases). All multidimensional injury maps were thresholded at 10% of the maximal intensity and overlaid on grayscale proton density images. Multidimensional injury maps of Subject 1 (control) show absent of significant injury under all experimental conditions. Multidimensional injury maps of Subject 2 (TBI) show substantial injury along the white-gray matter interface under all experimental conditions. Multidimensional injury maps of Subject 3 (TBI) show substantial injury at the bottom of the CC under all experimental conditions.

experimental conditions (e.g., unfiltered, filtered) and the co-registered APP density histological image as reference. All of the SSIM values are shown in Fig. S2 in the Supplementary Material. In the context of the current study we are most interested in the ability to accelerate the multidimensional MRI acquisition, and therefore the accuracy and quality of the reduced data cases are of particular importance. Compared with the unfiltered and reduced data injury biomarker maps, the SSIM values of the filtered and reduced data images increased by 11.1%, 0.9%, and 14.3% for the MD-$T_2$-based biomarker for Subjects 1 to 3, respectively, and increased by 8.6%, 7.7%, and 4.6% for the $T_1$-$T_2$-based biomarker for Subjects 1 to 3, respectively. All of these increases in SSIM were statistically significant ($p < 0.001$).

## 4 DISCUSSION

Here we report the use of the NESMA filter on multidimensional MRI data, in particular voxelwise $T_1$-$T_2$ and MD-$T_2$ spectra in fixed human Corpus Callosum, to remove noise and reduce total scan time. We focused on results from a recent study that identified potential imaging biomarkers of axonal injury pathology from the joint analysis of multidimensional MRI and histopathological data [20]. These axonal injury images were shown to be significantly and strongly correlated with histological evidence of axonal injury. Reprocessing these data provided an opportunity to test the performance of the NESMA filter and its effect on the accuracy of the injury biomarker maps, relative to the histological reference.

Our findings showed that noise reduction in the multidimensional MRI data using an adaptive nonlocal multispectral filter (i.e., NESMA [18]) improved the accuracy of the resulting injury biomarker maps, and furthermore, allowed for data reduction of 35.7% and 59.6% from the full dataset, which led to using only 36 and 122 images in the $T_1$-$T_2$ and MD-$T_2$ cases, respectively.

Specifically, visual inspection and a side-by-side comparison of the unfiltered and filtered subvoxel $T_1$-$T_2$ and MD-$T_2$ spectral components (Figs. 1, 2, and 3) showed that the filtered maps exhibit lower random variations, in particular at the lower ends of the spectra, and that there was no apparent loss of spectral information. For example, Subject 3 exhibited a relatively focal axonal injury at the bottom of the CC (Fig. 4, left panel), captured at the lower end of the $T_1$-$T_2$ spectra, which was previously associated with axonal injury [20]. Noticeable noise reduction at these spectral lower ends was observed, which is crucial to the robust identification of axonal injury from these multidimensional MRI data.

Our results suggest that the previously proposed [20] adaptive method of locating the injury-associated $T_1$-$T_2$-MD spectral signature is robust to noise removal procedures and to data reduction. Visual inspection of the resulting $T_1$-$T_2$ and MD-$T_2$ injury biomarker maps and the SSIM with respect to co-registered APP histological images suggest improved accuracy after applying the NESMA filter, even after the data was reduced (Figs. 4 and S2).

Multidimensional MRI is an emerging approach that is now being applied to address a range of medical conditions such as prediction of pregnancy complications via placenta characterization [9], spinal cord injury [6, 31], prostate cancer [32], breast cancer [33], and axonal injury due to TBI [20]. Recent *in vivo* proof-of-concept applications of subvoxel $T_1$-$T_2$ correlation spectra using 105 images [34] and of subvoxel diffusion-$T_1$ correlation spectra using 363 [11] and 304 [35] images are promising. Here we showed that accurate and robust subvoxel $T_1$-$T_2$ and MD-$T_2$ correlation spectra can be obtained using only 36 and 122 images, respectively, by using a constrained optimization data processing framework (i.e., MADCO [13]) in conjunction with applying the NESMA filter to reduce noise. A reliable and robust noise removal and consequent acquisition acceleration should further advance the field towards clinically-feasible diagnostic multidimensional MRI protocols.

## CONFLICT OF INTEREST STATEMENT

The authors declare that the research was conducted in the absence of any commercial or financial relationships that could be construed as a potential conflict of interest.

## AUTHOR CONTRIBUTIONS

DB: conceptualization, design of the study, methodology, software, investigation, data curation, writing—original draft, writing—review and editing, visualization, supervision, and project administration. MB: conceptualization, design of the study, methodology, software, and writing—review and editing. MK: methodology, investigation, and writing—review and editing. DI: methodology, investigation, and writing—review and editing. DP: investigation, methodology, resources, and writing—review and editing. DLB: design of the study, investigation, resources, and writing—review and editing. PB: conceptualization, methodology, resources, writing—review and editing, and funding acquisition. All authors contributed to the article and approved the submitted version.

## FUNDING

This research was partially supported by a grant from the U.S. Department of Defense, Program Project 308430 Uniformed Services University of the Health Sciences (USUHS). Support for this work also

included funding from the U.S. Department of Defense to the Brain Tissue Repository and Neuropathology Program, Center for Neuroscience and Regenerative Medicine (CNRM). DB and MEK were supported by the CNRM Neuroradiology- Neuropathology Correlations Core. MB was supported by the Intramural Research Program of the National Institute on Aging. DI, DPP, and DLB were supported by the CNRM and USUHS. PJB was supported by the Intramural Research Program of the Eunice Kennedy Shriver National Institute of Child Health and Human Development.

## ACKNOWLEDGMENTS

We thank the subjects' families that consented for brain donations for the better understanding of TBI consequences. The authors thank Mrs Patricia Lee, Mrs Nichelle Gray and Mr Paul Gegbeh for their valuable technical work. We are grateful to Mrs Stacey Gentile, Mrs Deona Cooper and Mr Harold Kramer Anderson for their administrative assistance. We thank the TRACK-TBI Investigators (https://tracktbi.ucsf.edu/transforming-research-and-clinical-knowledge-tbi).

The opinions expressed herein are those of the authors and are not necessarily representative of those of the Uniformed Services University of the Health Sciences (USUHS), the Department of Defense (DOD), the NIH or any other US government agency.

## SUPPLEMENTAL DATA

Supplementary material is available online.

## DATA AVAILABILITY STATEMENT

The datasets generated and analyzed during the current study are available from the corresponding author on reasonable request.

## REFERENCES

[1] English AE, Whittall KP, Joy MLG, Henkelman RM. Quantitative Two-Dimensional time Correlation Relaxometry. *Magnetic Resonance in Medicine* **22** (1991) 425–434.

[2] Hürlimann M, Flaum M, Venkataramanan L, Flaum C, Freedman R, Hirasaki G. Diffusion-relaxation distribution functions of sedimentary rocks in different saturation states. *Magnetic Resonance Imaging* **21** (2003) 305–310. doi:10.1016/S0730-725X(03)00159-0.

[3] Topgaard D. Multidimensional diffusion MRI. *Journal of Magnetic Resonance* **275** (2017) 98–113. doi:10.1016/j.jmr.2016.12.007.

[4] Benjamini D, Basser PJ. Multidimensional correlation MRI. *NMR in Biomedicine* (2020) e4226. doi:10.1002/nbm.4226.

[5] de Almeida Martins JP, Topgaard D. Two-Dimensional Correlation of Isotropic and Directional Diffusion Using NMR. *Physical Review Letters* **116** (2016) 087601.

[6] Kim D, Doyle EK, Wisnowski JL, Kim JH, Haldar JP. Diffusion-relaxation correlation spectroscopic imaging: A multidimensional approach for probing microstructure. *Magnetic Resonance in Medicine* **78** (2017) 2236–2249. doi:10.1002/mrm.26629.

[7] Benjamini D, Basser P. Water mobility spectral imaging of the spinal cord: Parametrization of model-free Laplace MRI. *Magnetic Resonance Imaging* **56** (2019).

[8] Benjamini D, Basser PJ. Magnetic resonance microdynamic imaging reveals distinct tissue microenvironments. *NeuroImage* **163** (2017) 183–196. doi:10.1016/j.neuroimage.2017.09.033.

[9] Slator PJ, Hutter J, Palombo M, Jackson LH, Ho A, Panagiotaki E, et al. Combined diffusion-relaxometry MRI to identify dysfunction in the human placenta. *Magnetic Resonance in Medicine* **82** (2019) 95–106. doi:10.1002/mrm.27733.

[10] de Almeida Martins JP, Tax CMW, Reymbaut A, Szczepankiewicz F, Chamberland M, Jones DK, et al. Computing and visualising intra-voxel orientation-specific relaxation–diffusion features in the human brain. *Human Brain Mapping* **42** (2021) 310–328.

[11] Reymbaut A, Critchley J, Durighel G, Sprenger T, Sughrue M, Bryskhe K, et al. Toward nonparametric diffusion- characterization of crossing fibers in the human brain. *Magnetic Resonance in Medicine* **85** (2021) 2815–2827.

[12] Benjamini D. Nonparametric Inversion of Relaxation and Diffusion Correlation Data. Topgaard D, editor, *Advanced Diffusion Encoding Methods in MRI* (Cambridge, UK: Royal Society of Chemistry), chap. 10 (2020), 278–316.

[13] Benjamini D, Basser P. Use of marginal distributions constrained optimization (MADCO) for accelerated 2D MRI relaxometry and diffusometry. *Journal of Magnetic Resonance* **271** (2016) 40–45. doi:10.1016/j.jmr.2016.08.004.

[14] Benjamini D, Basser PJ. Towards clinically feasible relaxation-diffusion correlation MRI using MADCO. *Microporous and Mesoporous Materials* **269** (2018) 93–96. doi:10.1016/j.micromeso.2017.02.001.

[15] Bai R, Cloninger A, Czaja W, Basser PJ. Efficient 2D MRI relaxometry using compressed sensing. *Journal of Magnetic Resonance* **255** (2015) 88–99.

[16] Hutter J, Slator PJ, Christiaens D, Teixeira RPAG, Roberts T, Jackson L, et al. Integrated and efficient diffusion-relaxometry using ZEBRA. *Scientific Reports* **8** (2018) 15138. doi:10.1038/s41598-018-33463-2.

[17] Bouhrara M, Bonny JM, Ashinsky BG, Maring MC, Spencer RG. Noise Estimation and Reduction in Magnetic Resonance Imaging Using a New Multispectral Nonlocal Maximum-likelihood Filter. *IEEE Transactions on Medical Imaging* **36** (2017) 181–193.

[18] Bouhrara M, Reiter DA, Maring MC, Bonny JM, Spencer RG. Use of the NESMA Filter to Improve Myelin Water Fraction Mapping with Brain MRI. *Journal of Neuroimaging* **28** (2018) 640–649.

[19] Bouhrara M, Lee DY, Rejimon AC, Bergeron CM, Spencer RG. Spatially adaptive unsupervised multispectral nonlocal filtering for improved cerebral blood flow mapping using arterial spin labeling magnetic resonance imaging. *Journal of Neuroscience Methods* **309** (2018) 121–131.

[20] Benjamini D, Iacono D, Komlosh ME, Perl DP, Brody DL, Basser PJ. Diffuse axonal injury has a characteristic multidimensional MRI signature in the human brain. *Brain* **144** (2021) 800–816.

[21] Johnson VE, Stewart W, Smith DH. Axonal pathology in traumatic brain injury. *Experimental Neurology* **246** (2013) 35–43. doi:10.1016/j.expneurol.2012.01.013.

[22] Pas K, Komlosh ME, Perl DP, Basser PJ, Benjamini D. Retaining information from multidimensional correlation MRI using a spectral regions of interest generator. *Scientific Reports* **10** (2020) 3246. doi:10.1038/s41598-020-60092-5.

[23] Provencher SW. A constrained regularization method for inverting data represented by linear algebraic or integral equations. *Computer Physics Communications* **27** (1982) 213–227. doi:10.1016/0010-4655(82)90173-4.

[24] Kroeker RM, Henkelman MR. Analysis of biological NMR relaxation data with continuous distributions of relaxation times. *Journal of Magnetic Resonance (1969)* **69** (1986) 218–235. doi:10.1016/0022-2364(86)90074-0.

[25] Song YQ, Venkataramanan L, Hürlimann M, Flaum M, Frulla P, Straley C. T1-T2 Correlation Spectra Obtained Using a Fast Two-Dimensional Laplace Inversion. *Journal of Magnetic Resonance* **154** (2002) 261–268. doi:10.1006/jmre.2001.2474.

[26] Mitchell J, Chandrasekera TC, Gladden LF. Numerical estimation of relaxation and diffusion distributions in two dimensions. *Progress in Nuclear Magnetic Resonance Spectroscopy* **64** (2012) 34–50. doi:10.1016/j.pnmrs.2011.07.002.

[27] Celik H, Bouhrara M, Reiter DA, Fishbein KW, Spencer RG. Stabilization of the inverse Laplace transform of multiexponential decay through introduction of a second dimension. *Journal of Magnetic Resonance* **236** (2013) 134–139. doi:10.1016/j.jmr.2013.07.008.

[28] Labadie C, Lee J, Vetek G, Springer C. Relaxographic Imaging. *Journal of Magnetic Resonance, Series B* **105** (1994) 99–112. doi:10.1006/jmrb.1994.1109.

[29] Bouhrara M, Maring MC, Spencer RG. A simple and fast adaptive nonlocal multispectral filtering algorithm for efficient noise reduction in magnetic resonance imaging. *Magnetic Resonance Imaging* **55** (2019) 133–139.

[30] Wang Z, Bovik A, Sheikh H, Simoncelli E. Image Quality Assessment: From Error Visibility to Structural Similarity. *IEEE Transactions on Image Processing* **13** (2004) 600–612.

[31] Benjamini D, Hutchinson EB, Komlosh ME, Comrie CJ, Schwerin SC, Zhang G, et al. Direct and specific assessment of axonal injury and spinal cord microenvironments using diffusion correlation imaging. *NeuroImage* **221** (2020) 117195.

[32] Zhang Z, Wu HH, Priester A, Magyar C, Afshari Mirak S, Shakeri S, et al. Prostate Microstructure in Prostate Cancer Using 3-T MRI with Diffusion-Relaxation Correlation Spectrum Imaging: Validation with Whole-Mount Digital Histopathology. *Radiology* **296** (2020) 348–355.

[33] Naranjo ID, Reymbaut A, Brynolfsson P, Lo Gullo R, Bryskhe K, Topgaard D, et al. Multidimensional Diffusion Magnetic Resonance Imaging for Characterization of Tissue Microstructure in Breast Cancer Patients: A Prospective Pilot Study. *Cancers* **13** (2021) 1606.

[34] Kim D, Wisnowski JL, Nguyen CT, Haldar JP. Multidimensional correlation spectroscopic imaging of exponential decays: From theoretical principles to in vivo human applications. *NMR in Biomedicine* **e4244** (2020). doi:10.1002/nbm.4244.

[35] Avram AV, Sarlls JE, Basser PJ. Whole-Brain Imaging of Subvoxel T1-Diffusion Correlation Spectra in Human Subjects. *Frontiers in Neuroscience* **15** (2021).